Journal of Molecular Structure 1100 (2015) 225–236

Contents lists available at ScienceDirect

Journal of Molecular Structure

journal homepage: http://www.elsevier.com/locate/molstruc

# Spectroscopic and electronic structure calculation of a potential chemotherapeutic agent 5-propyl-6-(*p*-tolylsulfanyl)pyrimidine-2,4(1*H*,3*H*)-dione using first principles

Monirah A. Al-Alshaikh [a], Omar A. Al-Deeb [b], Nourah Z. Alzoman [b], Ali A. El-Emam [b], Ruchi Srivastava [c], Alok K. Sachan [c], Onkar Prasad [c], Leena Sinha [c, *]

[a] Department of Chemistry, College of Sciences, King Saud University, Riyadh 11451, Saudi Arabia
[b] Department of Pharmaceutical Chemistry, College of Pharmacy, King Saud University, Riyadh 11451, Saudi Arabia
[c] Department of Physics, University of Lucknow, 226007 Lucknow, India

ARTICLE INFO

*Article history:*
Received 18 May 2015
Received in revised form
20 July 2015
Accepted 21 July 2015
Available online 26 July 2015

*Keywords:*
FT-IR
FT-Raman
NBO analysis
NLO properties
Pyrimidine-2,4(1*H*,3*H*)-dione

ABSTRACT

Quantum chemical calculations of energy, geometrical structure and vibrational wavenumbers of a potential chemotherapeutic agent namely, 5-propyl-6-(*p*-tolylsulfanyl)pyrimidine-2,4(1*H*,3*H*)-dione were carried out, using DFT method. Comprehensive interpretation of the experimental FT-IR and FT-Raman spectra of the compound under study is based on potential energy distribution. The difference between the observed and scaled wavenumbers of most of the normal modes is very small with B3LYP/6-311 + +G(d,p) method. The UV–Vis spectrum of the compound was recorded and the electronic properties, such as frontier orbitals and band gap energies were calculated by the TD-DFT approach. The values of the electric dipole moment, polarizability and first static hyperpolarizability of the title compound have also been investigated. NBO analysis has been performed to explain the charge transfer within the molecule along with the calculation of different thermo-dynamical properties.



## 1. Introduction

Due to multifarious pharmacological activities, pyrimidine and its related derivatives take up a key position in the field of chemotherapy. The chemotherapeutic efficacy of pyrimidine derivatives is related to their ability to inhibit vital enzymes responsible for DNA biosynthesis, such as dihydrofolate reductase, thymidylate synthetase, thymidine phosphorylase and reverse transcriptase. A broad set of pyrimidine drugs possesses a variety of curative properties. Several pyrimidine-based derivatives have been developed as anticancer agents [1–4], and antiviral agents against HIV [5–9], HBV [10,11], HCV [12], and HSV [13,14]. In addition, several pyrimidine derivatives have long been recognized as potent bactericidal [15–19], fungicidal [20,21] and antiprotozoal agents [22–25]. 1-[(2-Hydroxyethoxy)methyl]-6-(phenylthio) thymine (HEPT) and its related derivatives [26–30] were discovered as potent and selectively active agents against HIV–1 infections. In perpetuation to our pursuit in the structural and pharmacological properties of pyrimidine and uracil derivatives [8,9,18,31–35], the title compound was synthesized as the more lipophilic 5-propyl HEPT analog for evaluation as potential chemotherapeutic agent [36], which is expected to endow better pharmacokinetic properties. In the present study, we present an in-depth investigation on the molecular structure, electronic properties and vibrational spectra of the title compound (Molecular formula $C_{14}H_{16}N_2O_2S$), with the aspiration that the results of present study may be decisive in the prognosis of its mechanism of biological activity.

The experimental FT-IR and FT-Raman spectra of the title compound have been recorded and the explicit assignment of spectral peaks has been done using normal coordinate analysis. The inversion dimer connected through pairs of strong N–H…O hydrogen bonds has been studied by DFT/B3LYP at the 6-31 + G(d,p) level. The UV–Vis spectrum of the title compound was recorded and electronic properties, such as frontier orbitals and band gap energies were calculated by the TD-DFT approach. The study also comprises of calculation of the non-linear optical parameters, 2D molecular electrostatic potential (MESP) contour map and 3D MESP surface map accompanied by DOS and PDOS analysis

* Corresponding author.
*E-mail address:* sinhaleena27@gmail.com (L. Sinha).

http://dx.doi.org/10.1016/j.molstruc.2015.07.042
0022-2860/

of molecular orbitals. The Gauge-Including Atomic Orbital method has been used to calculate $^1$H nuclear magnetic resonance (NMR) chemical shifts of the compound and comparison has been made with observed experimental $^1$H NMR shifts. NBO analysis has been performed to explain the charge transfer within the molecule. Calculations of different thermo-dynamical properties have also been done.

## 2. Experimental details

The pure single colorless crystals of the title compound were synthesized in 72% yield via the reaction of 6-chloro-5-propyluracil with p-thiocresol in the presence of potassium hydroxide, and the structure was well established [36]. Perkin Elmer version 10.03.06 spectrophotometer was used for recording the FT-IR spectrum in the region 4000–400 cm$^{-1}$ using KBr pellet. The 532 nm laser light was used as the exciting wavelength for recording FT-Raman spectrum in the region 4000–50 cm$^{-1}$ using Planar RAME spectrometer. The UV absorption spectrum of the title compound was examined in the range 500–200 nm using UV-VIS Varian Cary 50 Bio spectrophotometer. The UV pattern is taken from a $10^{-5}$ M solution, dissolved in methanol. All the experimental spectra were recorded at the Indian Institute of Technology, Kanpur, India.

## 3. Computational details

The molecular geometry was built from the X-ray diffraction data without any constraints [36]. The structures of monomer and dimer were optimized using gradient-corrected DFT with Becke 3 exchange [37] and Lee–Yang–Parr correlation functions (B3LYP) [38] with 6-311 ++ G(d,p) basis set. The vibrational wavenumbers under harmonic approximation were calculated at the same level of theory and basis set. The nonexistence of negative vibrational wavenumber in the Gaussian output shows the stability of the structure. The final optimized geometry for the monomer and dimer of the title compound, along with the numbering scheme of the atoms are shown in Fig. 1. The Counterpoise (CP) correction method of Boys and Bernardi was used, to shun the artificially lowered energy of the dimer as well as overblown strength of the hydrogen bonds due to the basis set superposition error (BSSE) [39]. The dipole moment μ, mean polarizability $\alpha$ and first static hyperpolarizability (β) have been calculated using density functional theory method and Buckingham's definitions [40,41].

The α and β values of Gaussian output are in atomic units (a.u.) so they have been converted into electrostatic units (esu) (α; 1 a.u. = 0.1482 × $10^{-24}$ esu, β; 1 a.u. = 8.6393 × $10^{-33}$ esu.). The variation of thermodynamical properties such as heat capacity, entropy and enthalpy change with temperature have also been reckoned on the basis of vibrational analysis. Their correlation equations with temperature were fitted by quadratic formulas.

The $^1$H chemical shifts are calculated with the gauge-included atomic orbital (GIAO) approach [42,43] by applying the B3LYP/6–11 + G(d,p) method and compared with the experimental NMR spectrum [36]. The electronic properties such as HOMO and LUMO energies were determined by the TD-DFT approach. For analysis of molecular orbitals, density of state plots such as TDOS, PDOS have been drawn and analyzed. The 3D MESP and 2D contour map of title compound were drawn to access the most electron rich and electron deficient regions in the title compound. The theoretical UV–Vis spectrum has been computed by the TD-DFT method with 6–311++G(d,p) basis set for the gas phase and the solvent effect also has been taken into consideration by implementing IEFPCM model at the same level of theory. The natural bonding orbital (NBO) calculations [44] were accomplished using Gaussian 09 [45] package at the same level in order to figure out various second

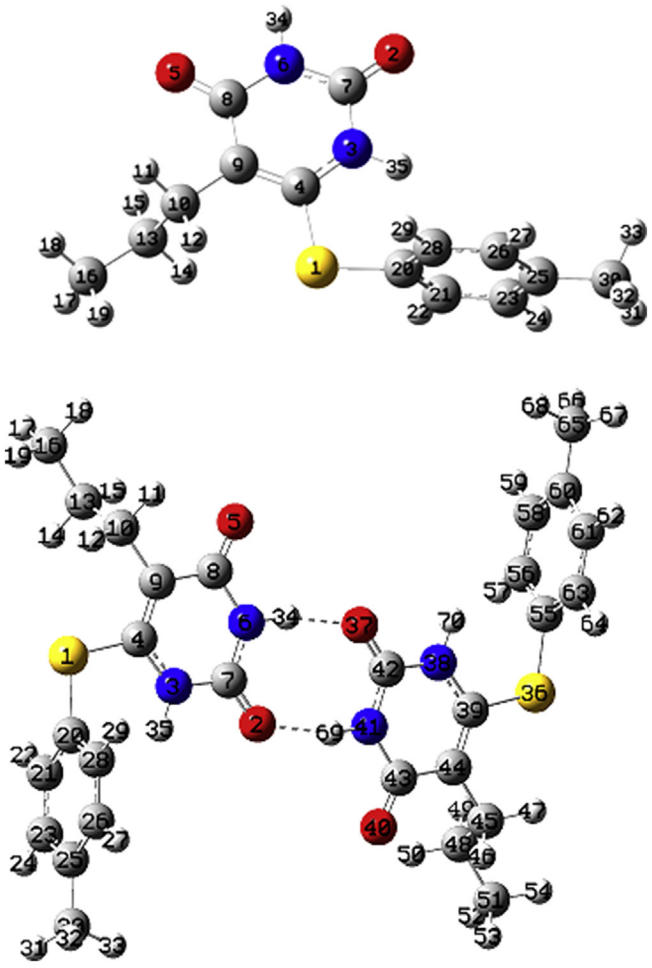

**Fig. 1.** Monomer and hydrogen bonded dimer of $C_{14}H_{16}N_2O_2S$.

order interactions between the filled orbitals of one subsystem and vacant orbitals of another subsystem, which enumerate the intramolecular delocalization or hyper conjugation. The interactions result in a loss of occupancy from the localized NBO of the idealized Lewis structure (occupancy = 2) into an empty non-Lewis orbital. For each donor (i) and acceptor (j), the stabilization energy $E^{(2)}$ associated with the delocalization i-j is estimated as

$$E^{(2)} = \Delta E_{ij} = q_i \frac{F(i,j)^2}{\varepsilon_j - \varepsilon_i}$$

where $q_i$ is the donor orbital occupancy, $\varepsilon_i$ and $\varepsilon_j$ are diagonal elements and F(i, j) is the off diagonal NBO Fock matrix element. The larger the $E^{(2)}$ value the more intensive is the interaction between electron donors and acceptors i.e., the more donation tendency from electron donors to electron acceptor and greater the extent of conjugation of the whole system [46]. The NBO analysis allows us to analyze the charge-transfers and intra-molecular bond paths. The vibrational wavenumber assignments were carried out by combining the animation option of the Gauss view 5.08 program [47,48] and MOLVIB program (version V7.0-G77; written by T. Sundius) [49–51]. An empirical uniform scaling factor of 0.983 up to 1700 cm$^{-1}$ and 0.958 for greater than 1700 cm$^{-1}$ [52,53] was used to offset the systematic errors caused by the basis set incompleteness and vibrational anharmonicity [54] and, in general, a good agreement of the calculated modes with the experimental

ones was obtained. The absolute Raman intensities were calculated from the Raman activities (Si), obtained with the Gaussian 09W program using the following relationship derived from the intensity theory of Raman scattering [55,56] according to the equation:

$$I_i = \left[f(\nu_0 - \nu_i)^4 S_i\right] \Big/ [\nu_i\{1 - \exp(-hc\nu_i/kT)\}]$$

where $\upsilon_0$ is the wavenumber in $cm^{-1}$ of the exciting light; $\upsilon_i$ is the vibrational wavenumber of the *i*th normal mode; *h*, *c* and *k* are universal constants; *f* is a suitably chosen common normalisation factor for all peak intensities. The calculated IR and Raman spectra were plotted using the pure Lorentzian band shape with a band width of FWHM of 10 $cm^{-1}$ along with the experimental spectra.

## 4. Results and discussion

### 4.1. Molecular geometry

The crystallographic information of the title compound shows that it crystallizes in a space group, $P2_1/c$ [36]. The crystal belongs to monoclinic system with the subsequent lattice parameters: a = 11.8356 Å, b = 10.3040 Å, c = 13.3999 Å, β = 119.850°, its unit cell volume being 1417.37 $Å^3$. The crystal structure of the title compound illustrates two kinds of intermolecular N–H…O hydrogen bonds. Two adjacent molecules form inversion-related dimers through strong N6–H34…O37 and N41–H69…O2 hydrogen bonds forming an eight membered ring motif [36]. These dimers are further connected into chains extending along *c* axis through additional N–HN…O hydrogen bonds [36]. These hydrogen bonding interactions contributes toward the crystal stability and form two-dimensional networks parallel to crystal *bc* plane. The hydrogen bond strength calculated using counterpoise (CP) correction method of Boys and Bernardi [39], is found to be 5.05596 kcal/mol (Interaction energy has been divided by a factor of 2 due to the formation of two similar hydrogen bonds formed). The counterpoise corrected energy and BSSE error has been calculated to be −2403.14198 a.u and 0.00124 a.u., respectively.

The calculated optimized geometrical parameters (bond lengths, bond angles and dihedral angles) of the title compound employing DFT-B3LYP/6–311++G(d,p) basis set along with the experimental X-ray data are listed in Table 1. The large difference in the theoretically-calculated value of the dihedral C4–S1–C20–C21 (−98.4°) with that of the experimental (−62.2°), led us to calculate potential energy scan, varying the aforesaid dihedral from −110° to −10°. The scan output (Fig. S1) reveals that in gas phase the lowest energy structure corresponds to the dihedral value around −100° and hence it is inferred that crystal forces and hydrogen bonding are playing a very dominant role in the real crystal structure in condensed phase. To ensure the stability of the optimized structure, PES scan has also been calculated varying the dihedral C4–C9–C10–C13 (Fig. S2). The minimum energy thus calculated corresponds to the dihedral at −95° and hence confirms the stability of the structure studied (dihedral C4–C9–C10–C13 = −94.4). The N–C bond lengths in the pyrimidine ring (1.378–1.408 Å) and the bridge C–S distances (1.788–1.797 Å) are comparable with those reported in the X-ray data. The optimized ground state energy of the title compound calculated using DFT-B3LYP method with 6–311++G(d,p) basis set found to be −1201.57169 Hartree. The C–H bond length in the p-tolylsulfanyl moiety varies in the range 1.086–1.097 Å. The two C=O bond lengths in the pyrimidine-2,4-dione ring are at 1.215 and 1.220 Å, where the C7=O2 is slightly shorter than the C8=O5, as both the Mulliken and natural charge analysis predict the O2 to be slightly higher than the O5 (Table S1).

**Table 1**
Computed optimized geometrical parameters of $C_{14}H_{16}N_2O_2S$ at B3LYP/6–311++G (d,p) level along with experimental values.

| Bond length (Å) | Exp[a] | Cal. | Bond angle (°) | Exp[a] | Cal. |
|---|---|---|---|---|---|
| S1–C4 | 1.766 | 1.788 | H15–C13–C16 | 109.3 | 109.7 |
| S1–C20 | 1.777 | 1.797 | C13–C16–H17 | 109.5 | 111.2 |
| O2–C7 | 1.225 | 1.215 | C10–C13–C16 | 111.6 | 112.4 |
| N3–C4 | 1.378 | 1.382 | S1–C20–C21 | 121.7 | 119.9 |
| N3–C7 | 1.361 | 1.389 | S1–C20–C28 | 117.8 | 120.5 |
| N3–H35 | 0.790 | 1.012 | C21–C20–C28 | 120.2 | 119.5 |
| C4–C9 | 1.350 | 1.366 | C20–C21–H22 | 120.3 | 119.8 |
| O5–C8 | 1.220 | 1.220 | C20–C21–C23 | 119.5 | 120.0 |
| N6–C7 | 1.358 | 1.378 | C21–C23–H24 | 119.3 | 119.2 |
| N6–C8 | 1.382 | 1.408 | C21–C23–C25 | 121.3 | 121.2 |
| N6–H34 | 0.840 | 1.013 | H24–C23–C25 | 119.3 | 119.6 |
| C8–C9 | 1.454 | 1.463 | C23–C25–C26 | 118.1 | 118.2 |
| C10–C13 | 1.509 | 1.544 | C23–C25–C30 | 120.8 | 121.2 |
| C13–H14 | 0.970 | 1.098 | C26–C25–C30 | 121.2 | 120.7 |
| C13–H15 | 0.970 | 1.096 | C25–C26–H27 | 119.1 | 119.5 |
| C13–C16 | 1.526 | 1.532 | C25–C26–C28 | 121.8 | 121.3 |
| C16–H17 | 0.960 | 1.095 | H27–C26–C28 | 119.1 | 119.2 |
| C20–C21 | 1.385 | 1.401 | C20–C28–C26 | 119.0 | 119.9 |
| C20–C28 | 1.379 | 1.404 | C20–C28–H29 | 120.5 | 119.8 |
| C21–H22 | 0.930 | 1.086 | C25–C30–H31 | 109.5 | 111.5 |
| C21–C23 | 1.378 | 1.397 | C25–C30–H32 | 109.5 | 111.3 |
| C23–C25 | 1.381 | 1.402 | C25–C30–H33 | 109.5 | 110.8 |
| C25–C26 | 1.378 | 1.405 | Bond dihedral (°) | | |
| C25–C30 | 1.508 | 1.510 | S1–C20–C28–C26 | 174.8 | 177.1 |
| C26–C28 | 1.383 | 1.394 | C20–S1–C4–N3 | −19.6 | 10.5 |
| C28–H29 | 0.930 | 1.086 | C20–S1–C4–C9 | 162.2 | −170.9 |
| Bond angle (°) | | | C4–S1–C20–C21 | −62.2 | −98.4 |
| C8–C9–C10 | 117.6 | 117.4 | C4–S1–C20–C28 | 123.2 | 85.5 |
| C4–S1–C20 | 104.5 | 103.4 | C7–N3–C4–C9 | −2.7 | 0.3 |
| C4–N3–C7 | 122.7 | 124.4 | C4–N3–C7–2O | −176.2 | 179.6 |
| C4–N3–H35 | 122.9 | 120.5 | C4–N3–C7–N6 | 3.3 | −0.5 |
| C7–N3–H35 | 114.1 | 115.1 | S1–C4–C9–C8 | −179.7 | −178.3 |
| S1–C4–N3 | 11.3 | 117.6 | S1–C4–C9–C10 | −0.1 | −0.6 |
| S1–C4–C9 | 119.8 | 120.7 | N3–C4–C9–C10 | −178.3 | 179.2 |
| N3–C4–C9 | 121.9 | 121.6 | C8–N6–C7–O2 | 175.7 | −180.0 |
| C7–N6–C8 | 126.5 | 127.3 | C8–N6–C7–N3 | −3.8 | 0.2 |
| C7–N6–H34 | 114.9 | 116.3 | C7–N6–C8–O5 | −176.3 | 179.9 |
| C8–N6–H34 | 118.3 | 116.4 | C7–N6–C8–C9 | 3.4 | 0.3 |
| O2–C7–N3 | 122.1 | 122.5 | O5–C8–C9–C4 | 177.4 | 179.9 |
| O2–C7–N6 | 122.8 | 124.4 | O5–C8–C9–C10 | −2.2 | 0.9 |
| N3–C7–N6 | 115.2 | 113.1 | N6–C8–C9–C4 | −2.3 | −0.5 |
| O5–C8–N6 | 119.3 | 119.4 | N6–C8–C9–C10 | 178.1 | −179.5 |
| O5–C8–C9 | 125.2 | 125.0 | C4–C9–C10–C13 | −99.1 | −94.4 |
| N6–C8–C9 | 115.6 | 115.6 | C8–C9–C10–C13 | 80.5 | 84.50 |
| C4–C9–C8 | 118.0 | 118.0 | C9–C10–C13–C16 | 174.6 | −178.9 |
| C4–C9–C10 | 124.4 | 124.5 | S1–C20–C21–C23 | −176.4 | −176.9 |
| | | | C28–C20–C21–C23 | −2.0 | −3.0 |
| | | | C21–C20–C28–C26 | 0.1 | 1.0 |
| | | | C20–C21–C23–C25 | 1.8 | 0.0 |
| N41–H69···O2 | 2.0 | 1.9 | C21–C23–C25–C26 | 0.3 | 0.5 |
| N6–H34···O37 | 2.2 | 1.9 | C21–C23–C25–C30 | −178.5 | −178.7 |
| | | | C23–C25–C26–C28 | −2.2 | −0.3 |
| | | | C30–C25–C26–C28 | 176.6 | 178.9 |

[a] Taken from Ref. [15].

### 4.2. Electronic properties and UV studies

To explore the interaction of the title compound with other species we have calculated the energy and composition of the most significant parameters of quantum chemistry – HOMO (highest occupied molecular orbital) and LUMO (lowest unoccupied molecular orbital). Energies of HOMO and LUMO are directly related to both the ionization potential and electron affinity. The energy gap between HOMO and LUMO is a noteworthy parameter to envisage molecular electrical transport properties as it is a measure of electron conductivity. The frontier orbital gap also helps to characterize the chemical reactivity and kinetic stability of the

molecule. A molecule with a small frontier orbital gap indicates its polarizable nature and is generally linked with a high chemical reactivity, low kinetic stability and such a molecule is termed as soft molecule [57]. Fully optimized ground state structure has been used at TD-DFT/B3LYP/6–311++G (d, p) level of theory to determine energies (Table 2) and plots (Fig. 2) of HOMO (MO 73), LUMO (MO 74) and other important MOs involved in the transitions of title compound. From Fig. 2, it is clear that HOMO is localized over the pyrimidine ring, sulfur atom and the propyl group and LUMO is localized over the sulfur atom and phenyl ring showing significant π anti-bonding character. The simulated UV spectrum and correlated properties such as vertical excitation energies (E), oscillator strengths (f) and the corresponding absorption wavelengths (λ) were computed for the gas phase and in methanol solvent (Table 3), and compared with the experimental UV spectrum. The calculations predict one intense electronic transition at 261.26/268.58 nm with an oscillator strength 0.2621/0.4079 corresponding to the gas phase/methanol solvent, in agreement with the measured experimental value (λ = 294.00 nm in methanol) as shown in Fig. 3. This electronic absorption corresponds to the transition from the molecular orbital HOMO (73) to LUMO (74) in methanol solvent and is a $\pi \rightarrow \pi^*$ transition. The peak in the calculated UV spectrum in gas phase arises mainly due to the electronic transition given by H→L+2. The energy gap (ΔE) of HOMO-LUMO/HOMO-LUMO+1/HOMO-LUMO+2 of the title molecule have found to be 4.77058/5.01275/5.20867 eV, respectively. The molecular electrostatic potential map (MESP) (electrostatic potential mapped onto an electron iso-density surface) may be used to predict reactive sites for electrophilic attack (electron rich region) and nucleophilic attack (electron poor region) and to investigate the correlation between the physiochemical properties and molecular structure of molecular systems including bio molecules and drugs [58–63]. The red and blue region refers to electron rich and electron poor region, respectively, while the green region in the MESP suggests almost neutral region. The MESP of the title compound (Fig. 4.) clearly shows the major negative potential region around the oxygen atoms attached to the pyrimidine ring with slight brunt of red region around bridged sulfur atom and the major positive region around tolyl moiety recognized by blue color. The blue region around the hydrogen attached with nitrogen atoms in the pyrimidine ring also suggests electron deficient region. The total density of states (TDOS) and partial density of states (PDOS) were drawn (Fig. 5) using the Gauss-Sum 2.2 Program [64] to represent makeup of the molecular orbital in the particular energy range, percentage contribution of a group to each molecular orbital. The PDOS plot clearly predicts major contribution to HOMO (almost 70%) comes from the pyrimidine-2,4-dione moiety, while the contribution from the tolysulfanyl and propyl groups is 22% and 8%, respectively. There is no contribution from the propyl group to LUMO, the 90% contribution comes from tolysulfanyl moiety and 10% from the pyrimidine-2,4-dione moiety.

**Table 2**
Calculated important orbital's energies (eV), energy differences between transition levels of studied molecule $C_{14}H_{16}N_2O_2S$.

| Parameters | TD-DFT/B3LYP/6–311++G(d,p) | |
|---|---|---|
| | Gas | Methanol |
| $E_{total}$(a.u.) | −1201.5717 | −1201.5869 |
| $E_{total}$(eV) | −32695.6067 | −32696.0193 |
| $E_{LUMO+2}$ (eV) | −1.1799 | −0.9423 |
| $E_{LUMO+1}$ (eV) | −1.3758 | −1.2833 |
| $E_{LUMO}$(eV) | −1.6180 | −1.3782 |
| $E_{HOMO}$(eV) | −6.3885 | −6.4585 |
| $\Delta E_{(HOMO-LUMO)}$ (eV) | 4.7706 | 5.0802 |
| $\Delta E_{(HOMO-LUMO+1)}$ (eV) | 5.0128 | 5.1752 |
| $\Delta E_{(HOMO-LUMO+2)}$ (eV) | 5.2087 | 5.5162 |
| HOMO (MO 73); LUMO (MO 74) | | |

$C_{14}H_{16}N_2O_2S$ dimer at DFT-B3LYP/6–31+G(d, p).
Counterpoise: corrected energy (a.u.) = −2403.14198.
Counterpoise: BSSE energy (a.u.) = 0.00124.
Interaction energy (a.u.) = 0.01611.

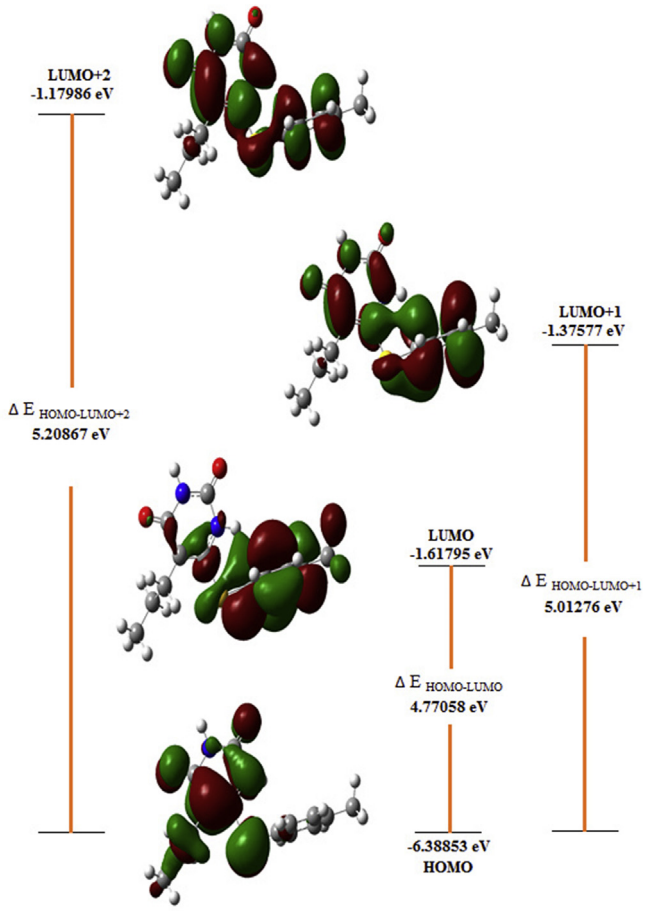


**Fig. 2.** Patterns of the HOMO, LUMO and other important Molecular Orbitals of the title compound.

**Table 3**
Experimental and calculated absorption wavelength λ (nm), excitation energies E (eV), absorbance values and oscillator strengths (f) of $C_{14}H_{16}N_2O_2S$.

| Experimental | | | TD-DFT/B3LYP/6–311++G(d,p) | | |
|---|---|---|---|---|---|
| λ (nm) | E (eV) | Abs. | λ (nm) | E (eV) | *f* |
| Gas phase | | | | | |
| | | | 307.36(73 → 74) | 4.0339 | 0.0034 |
| | | | 280.48(73 → 75) | 4.4204 | 0.0176 |
| | | | 261.26(73 → 76) | 4.7457 | 0.2640 |
| | | | 255.75(72 → 76) | 4.8479 | 0.0679 |
| | | | 241.87(70 → 74) | 5.1261 | 0.0064 |
| | | | 237.98(73 → 77) | 5.2099 | 0.0076 |
| Methanol | | | | | |
| | | | 282.83(73 → 75) | 4.3838 | 0.0148 |
| 294.00 | 4.2259 | 0.443 | 268.58(73 → 74) | 4.6163 | 0.4079 |
| | | | 253.77(73 → 76) | 4.8858 | 0.0487 |
| | | | 245.89(70 → 74) | 5.0423 | 0.0073 |
| | | | 240.80(72 → 76) | 5.1489 | 0.0033 |
| | | | 231.88(72 → 74) | 5.3470 | 0.0071 |

### 4.3. Electric moments

The electric moments such as dipole moment, polarizability,

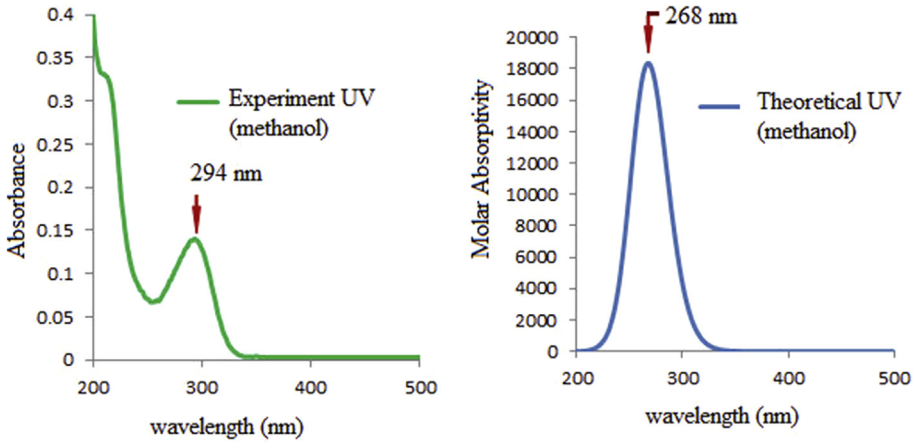


**Fig. 3.** Experimental and simulated UV absorption spectra of $C_{14}H_{16}N_2O_2S$.

hyperpolarizability of the title compound have been calculated at the DFT-B3LYP/6–311++G(d,p) level of theory to predict its nonlinear properties. The dipole moment illustrating the net molecular polarity is calculated to be 6.626 Debye (Table 4). The small frontier orbital energy gap and high dipole moment of the title compound show its high activity and less stability. The polarizability and first static hyperpolarizability of the title compound are found to be 215.31 a.u. ($31.909 \times 10^{-24}$ e.s.u.) and $3.378 \times 10^{-30}$ e.s.u., respectively, with their components listed in Table 4.

### 4.4. Thermodynamic properties

On the basis of vibrational analysis, the statistical thermodynamic functions: heat capacity ($C^0_{p,m}$), entropy ($S^0_m$) and enthalpy ($H^0_m$) changes for title compound were obtained from theoretical harmonic wavenumbers and listed in Table S2. It can be observed that these thermodynamic functions are directly proportional to temperature in the range 100–700 K and their corresponding fitting equations are as follows with the correlation graphics shown in Fig. 6.

$$S^0_m = 66.81 + 0.295\,T - 8 \times 10^{-5}T^2 \quad \left(R^2 = 0.999\right)$$

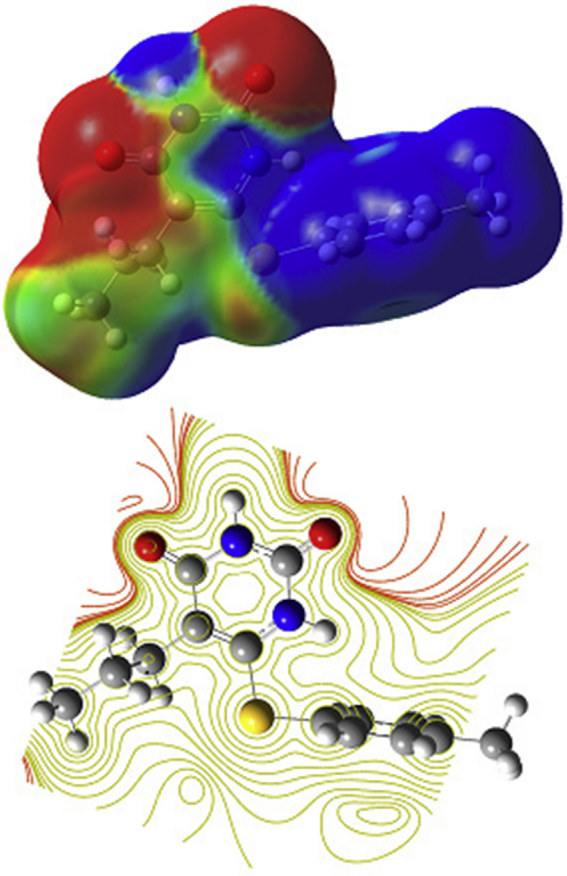

**Fig. 4.** 3D MESP and 2D contour map of $C_{14}H_{16}N_2O_2S$.

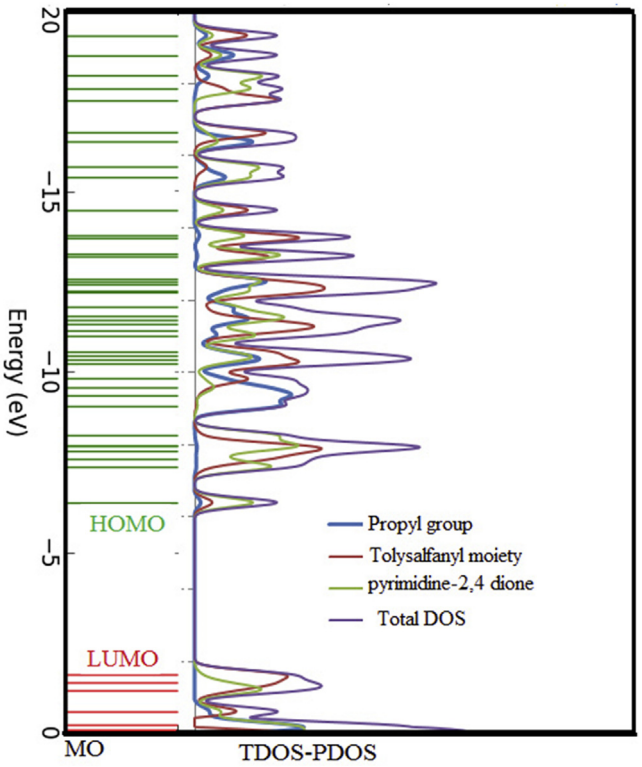


**Fig. 5.** TDOS and PDOS plots for the title compound.

$$C^0_{p,m} = 6.299 + 0.242\,T - 9\times10^{-5}T^2 \quad (R^2 = 0.999)$$

$$\Delta H^0_m = -0.835 + 0.019T + 9\times10^{-5}T^2 \quad (R^2 = 0.999)$$

The thermodynamic data presented here may be used to compute other thermodynamic energies according to the relationships of thermodynamic functions and estimate guidelines of chemical reactions according to the second law of thermodynamics in Thermochemical field [65]. As all the thermodynamic calculations were done in gas phase, they could not be used in solution.

### 4.5. NMR studies

The NMR spectroscopy is currently used for structure and functional determination of biological macromolecules. Recent advances in experimental and computational techniques have made it possible to exploit the NMR chemical shifts to obtain the structures of proteins and macromolecules [66]. The optimized structure of title compound was used to simulate $^1$H NMR spectra of the compound at the DFT-B3LYP/6−311++G(d, p) level using the Gauge-Including Atomic Orbital (GIAO) method in which an exponential term containing the vector potential is included with each atomic orbital. The calculated $^1$H chemical shifts for the title compound in the gas phase as well as in DMSO solvent, taking tetrarmethylsilane (TMS) as a reference, is given in Table 5, along with experimentally-observed values [36]. The H34 and H35 atoms attached to the nitrogen atoms of the pyrimidine ring show downfield NMR signal at 11.21 and 10.74 ppm in DMSO with theoretical value at 6.72 and 5.77 ppm, respectively. The deviation in the theoretical and experimental values may be due to the fact that the hydrogen atoms are involved in strong hydrogen bonding. The three equivalent hydrogen (H31, H32, H33) of the $CH_3$ group of tolysulfanyl moiety and other three equivalent (H17, H18, H19) hydrogen of propyl group show NMR signals at 2.31 and 0.84 ppm, respectively, matched well with the theoretical values. The chemical shifts for other hydrogen atoms are in good correlation with the experimental values.

### 4.6. Natural bond orbital (NBO) analysis

The natural bond orbital analysis gives the exact possible natural Lewis structure picture. The NBO analysis explains the conjugative interaction in a molecular system. The interactions between both filled and virtual orbital spaces are correctly explained by the NBO analysis. The delocalization of electron density between occupied Lewis type (bond or lone pair) NBO orbital and formally unoccupied (antibond or Rydgberg) non-Lewis NBO orbital corresponds to a stabilizing donor−acceptor interaction. The NBO analysis has been performed on the title compound at the DFT/B3LYP/6−311++G(d,p) level in order to elucidate charge transfers or conjugative interaction, the intra-molecule re-hybridization and delocalization of electron density within the molecule. The second order perturbation theory analysis of Fock matrix in the NBO basis of the molecule shows the strong intra-molecular hyper conjugative interactions which are presented in Table S3. The strong intra-molecular hyper conjugative interaction of π(C4−C9) to π*(O5−C8) of pyrimidine ring with energy 22.24 kcal/mol and the charge transfer from π(C23−C25) to π*(C26−C28)/π*(C20−C21) amounts to the stabilization of 18.28/25.94 kcal/mol. The important interactions involving the lone pair of N3(1) with that of anti-bonding π*(O2−C7)/π* (C4−C9) and the lone pair of N6(1) with the anti-bonding π*(O2−C7) and π*(O5−C8) results in stabilization of the system by 53.21/41.41 kcal/mol and 60.2/48.45 kcal/mol, respectively. The lone pairs LP(1)N3 and LP(1)N6 having 99.99% p-character, are occupied by 1.6612 and 1.6522 e electrons, respectively, (consistent with a delocalization of electron density from the idealized Lewis occupancy of 2.0 electrons). The direction of the line of centers between the two nuclei is compared with the hybrid direction to determine the bending of the bond, expressed as the deviation angle (Dev) between these two directions. The hybrid directionality and bond bending analysis of natural hybrid orbital's (NHOs) offer indications of the substituent effect and the steric effect. It is evident from Table 6 that the C4 NHOs of σ (S1−C4) are away from the line of center by 3.9°, whereas the S1 and C20 NHOs of σ (S1−C20) are away from their line of centers by 1.5° and 3.4°, respectively.

### 4.7. Vibrational analysis

The title compound has C1 symmetry and 35 atoms that give rise to 99 normal modes of vibrations, which are described in detail with the help of normal coordinate analysis. The specific assignment to each vibration is attempted using the potential energy distribution (PED). For this purpose, the full set of internal coordinates is given in Table S4. To obtain the normal modes, the local symmetry coordinates as recommended by Fogarasi and Pulay are defined and presented in Table S5. This method is also valuable for determining the mixing of other modes, where the maximum contribution is agreed to be the most significant mode. The observed FT-Raman and FT-IR bands with their relative intensities, calculated wavenumbers and assignments are given in Table 7. The

**Table 4**
Dipole moment, polarizability and first hyperpolarizability data for $C_{14}H_{16}N_2O_2S$ calculated at B3LYP/6−311++G(d,p).

| Dipole Moment | | | Polarizability[a] | | Hyperpolarizability[b] | | |
|---|---|---|---|---|---|---|---|
| | | | a.u. | esu ( × $10^{-24}$) | | a.u. | esu ( × $10^{-33}$) |
| $\mu_x$ | 5.839 | $\alpha_{xx}$ | 303.77 | 45.018 | $\beta_{xxx}$ | −94.793 | −818.946 |
| $\mu_y$ | −3.132 | $\alpha_{xy}$ | 9.09 | 1.347 | $\beta_{xxy}$ | 123.614 | 1067.940 |
| $\mu_z$ | −0.001 | $\alpha_{yy}$ | 187.32 | 27.761 | $\beta_{xyy}$ | −307.650 | −2657.880 |
| $\mu_{total}$(D) | 6.626 | $\alpha_{xz}$ | −7.93 | −1.175 | $\beta_{yyy}$ | 81.989 | 708.323 |
| | | $\alpha_{yz}$ | 0.16 | 0.024 | $\beta_{xxz}$ | −8.659 | −74.803 |
| | | $\alpha_{zz}$ | 154.84 | 22.948 | $\beta_{xyz}$ | 21.387 | 184.766 |
| | | $\alpha_{mean}$ | 215.31 | 31.909 | $\beta_{yyz}$ | 19.427 | 167.834 |
| | | | | | $\beta_{xzz}$ | 29.705 | 256.628 |
| | | | | | $\beta_{yzz}$ | −89.631 | −774.352 |
| | | | | | $\beta_{zzz}$ | 10.484 | 90.571 |
| | | | | | $\beta_{tot}$ | 390.941 | 3377.456 |
| | | | | | $\beta_{tot}$ ( × $10^{-30}$ esu) | | 3.378 |

[a] In atomic units Conversion factor to the SI units, 1 $e^2a_0^2E_h^{-1} = 1.648778\times10^{-41}$ $C^2$ $m^2$ $J^{-1}$.
[b] In atomic units Conversion factor to the SI units, 1 $e^3a_0^3E_h^{-2} = 3.206361\times10^{-53}$ $C^3$ $m^3$ $J^{-2}$.

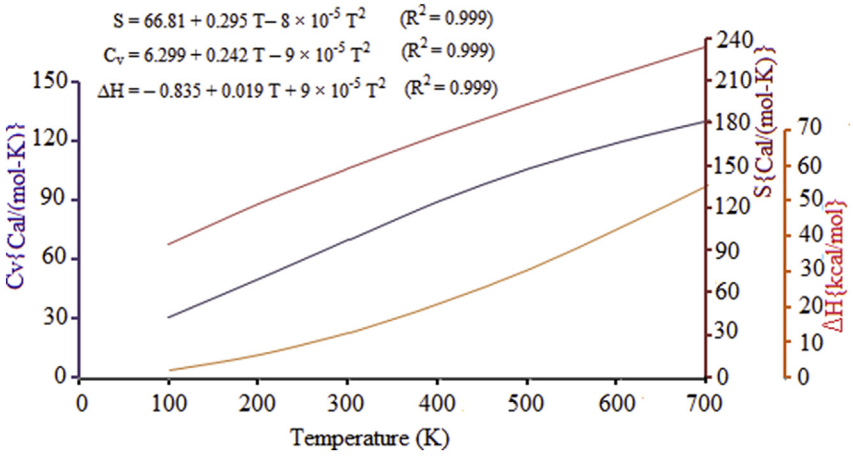


**Fig. 6.** Correlation graphs of calculated heat capacity, entropy and change in enthalpy for $C_{14}H_{16}N_2O_2S$.

**Table 5**
The observed (in Gas phase and DMSO solvent) and calculated isotropic proton chemical shifts for $C_{14}H_{16}N_2O_2S$ with respect to TMS.

| Atom | Exp.(a) | 6-311++G(d,p) | |
|---|---|---|---|
| | | Gas | DMSO |
| H11 | 2.44 | 2.64 | 2.50 |
| H12 | 2.44 | 1.89 | 2.08 |
| H14 | 1.38 | 1.18 | 1.30 |
| H15 | 1.40 | 1.55 | 1.41 |
| H17 | 0.84 | 1.13 | 1.16 |
| H18 | 0.84 | 0.92 | 0.88 |
| H19 | 0.84 | 0.79 | 0.88 |
| H22 | 7.30 | 7.73 | 7.83 |
| H24 | 7.30 | 7.39 | 7.58 |
| H27 | 7.22 | 7.54 | 7.72 |
| H29 | 7.22 | 7.64 | 7.72 |
| H31 | 2.31 | 2.12 | 2.23 |
| H32 | 2.31 | 2.35 | 2.43 |
| H33 | 2.31 | 2.64 | 2.66 |
| H34 | 11.21 | 6.58 | 6.72 |
| H35 | 10.74 | 5.53 | 5.77 |

**Table 6**
NHO directionality and 'bond bending' (deviations from line of nuclear centres).

| Bond (A-B) | Deviation at A (°) | Deviation at B (°) |
|---|---|---|
| S1–C4 | – | 3.9 |
| S1–C20 | 1.5 | 3.4 |
| O2–C7 | 1.4 | 1.5 |
| N3–C37 | 1.3 | – |
| N3–H35 | 1.1 | – |
| N6–C7 | 2.1 | 1.1 |
| N6–C8 | 2.0 | 1.3 |
| C8–C9 | 1.3 | – |
| C9–C10 | 1.1 | 1.8 |
| C10–H12 | 1.2 | – |
| C10–C13 | 1.6 | – |
| C13–C16 | 1.1 | – |
| C16–H18 | 1.3 | – |
| C16–H19 | 1.5 | – |
| C20–C21 | 2.5 | – |
| C20–H28 | 2.3 | – |
| C21–C23 | 1.1 | 1.1 |
| C26–C28 | 1.2 | 1.2 |
| C30–H32 | 1.0 | – |
| C30–H33 | 1.3 | – |

experimental FT-IR and FT-Raman spectra with the corresponding theoretically-simulated IR and Raman spectra are shown in Fig. 7 and Fig. 8, respectively. For complete vibrational analysis of the title compound, the vibrational modes are discussed under the headings- Pyrimidine Ring vibrations, C–S bridge vibrations, C=O vibrations, Phenyl Ring vibrations, $CH_2$ vibration and Methyl group vibrations.

*4.7.1. Pyrimidine ring vibrations*

Strong absorption in the range 1600–1500 $cm^{-1}$ is marked in the spectra of pyrimidines due to the C=N and C=C stretching vibrations [67]. The C=C stretching vibration for 2-trifluoromethyl-10H-benzo[4,5]imidazo[1,2-a]pyrimidin-4-one has been observed by Sert et al. [68]. at 1609, 1590 and 1556 $cm^{-1}$ in the IR and at 1612, 1588 and 1559 $cm^{-1}$ in the Raman spectrum, whereas, the C=N stretching modes have been observed at 1609, 1590 $cm^{-1}$ in the IR and 1612 and 1588 $cm^{-1}$ in the Raman spectrum. For the title compound, the characteristic pyrimidine C=C stretching mode is observed at 1623/1584 $cm^{-1}$ in FT-IR/FT-Raman spectrum. A strong peak at 1582 $cm^{-1}$ in FT-IR spectrum have contribution from C=C as well as C=N stretch. The ring breathing and trigonal bending modes of the pyrimidine ring are two very interesting modes that show characteristic peaks in the Raman spectrum of pyrimidine and its derivatives. Barnes et al. [69] identified strong Raman band at 760 $cm^{-1}$ as the ring breathing mode for uracil. Yadav et al. [70] have observed the ring breathing mode at 718/724 $cm^{-1}$ and the triagonal ring bending mode at 858/859 $cm^{-1}$ in the FT-Raman/FT-IR spectra of 2-thiocytosine. Bayrak [71].has reported ring breathing mode in 2-amino-4-methylpyrimidine tetracyanonickelate complex at 988 $cm^{-1}$. Singh et al. [72] have reported hydrogen bonding in different pyrimidine-methanol clusters probed by polarized Raman spectroscopy and DFT calculations and found the ring breathing mode for neat pyrimidine at 1011.2 $cm^{-1}$. In the present investigation, the peak at 885 $cm^{-1}$ in the FT-IR and 894 $cm^{-1}$ in the FT-Raman spectrum are assigned to the ring breathing mode of pyrimidine, which corresponds to the theoretical peak at 881 $cm^{-1}$. These data on various pyrimidine derivatives suggests that the ring breathing mode is highly sensitive to the substitution, interactions and environment. Trigonal ring bending mode is calculated at 999 $cm^{-1}$, and corresponding observed peak in the experimental spectra is at 1018 $cm^{-1}$. The C–C–C in-plane bending vibrations are generally observed around 600 $cm^{-1}$ [73,74]. The observed band in FT-IR/FT-Raman spectra at 580/595, 526/528 and 436/443 $cm^{-1}$ are assigned to the C–C–C in-plane bending vibrations which are in good coherence with the theoretical spectra.

The N–H stretching vibration of the heterocyclic compounds appears in the region of 3500–3000 $cm^{-1}$ [46]. A broad band at

**Table 7**
Comparison of experimental infrared wavenumbers ($cm^{-1}$) with theoretical harmonic frequencies ($cm^{-1}$), infrared intensities, Raman scattering activities and Raman intensities of molecule $C_{14}H_{16}N_2O_2S$ along with the assignments of vibrational modes basing on PED results.

| S. No. | Experimental wavenumbers | | Calculated wavenumbers | | IR intensity | Raman Activity | Raman intensity | Assignment of dominant modes (PED below 10% not taken in to the consideration) |
|---|---|---|---|---|---|---|---|---|
| | FT-IR | Raman | Unscaled | Scaled | | | | |
| 1 | 3222 bb | 3225 | 3604 | 3452 | 68.5 | 120.5 | 193.5 | νNH(R1) (100) |
| 2 | | | 3596 | 3445 | 199.3 | 73.6 | 118.7 | νNH(R1) (100) |
| 3 | 3161 m | 3058 m | 3193 | 3059 | 0.4 | 177.3 | 355.5 | νCH(R2) (99) |
| 4 | | 3054 m | 3191 | 3057 | 4.6 | 7.9 | 15.8 | νCH(R2) (99) |
| 5 | 3035 m | | 3168 | 3035 | 9.6 | 97.3 | 197.9 | νCH(R2) (99) |
| 6 | 3033 m | | 3166 | 3033 | 8.8 | 101.3 | 206.2 | νCH(R2) (99) |
| 7 | | | 3110 | 2980 | 13.1 | 71.3 | 149.7 | $\nu CH(30C)_{as1}$ (91) |
| 8 | | | 3088 | 2958 | 47.8 | 58.6 | 124.8 | $\nu CH(16C)_{as2}$ (36) + $\nu CH(16C)_{as1}$ (28) + $\nu CH(13C)_{as}$ (20) + $\nu CH(10C)_{as}$ (15) |
| 9 | 2957w | | 3086 | 2956 | 48.4 | 93.7 | 199.7 | $\nu CH(16C)_{as1}$ (69) + $\nu CH(13C)_{as}$ (27) |
| 10 | 2953w | | 3082 | 2953 | 14.1 | 96.9 | 206.7 | $\nu CH(30C)_{as2}$ (89) |
| 11 | | | 3072 | 2943 | 2.6 | 7.4 | 15.9 | $\nu CH(10C)_{as}$ (56) + $\nu CH(16C)_{as2}$ (38) |
| 12 | | | 3054 | 2926 | 4.9 | 102.9 | 223.2 | $\nu CH(13C)_{as}$ (53) + $\nu CH(16C)_{as2}$ (28) + $\nu CH(10C)_{as}$ (11) |
| 13 | | | 3029 | 2902 | 32.5 | 63.4 | 139.4 | $\nu CH(10C)_{ss}$ (65) + $\nu CH(13C)_{ss}$ (13) + $\nu CH(13C)_{as}$ (10) + $\nu CH(10C)_{as}$ (10) |
| 14 | 2925w | 2919s | 3028 | 2901 | 19.6 | 340.7 | 749.9 | $\nu CH(30C)_{ss}$ (93) |
| 15 | | | 3020 | 2894 | 5.7 | 158.4 | 350.1 | $\nu CH(13C)_{ss}$ (83) + $\nu CH(10C)_{ss}$ (10) |
| 16 | 2852 m | 2866s | 3018 | 2891 | 33.9 | 159.6 | 353.4 | $\nu CH(16C)_{ss}$ (96) |
| 17 | 1709 m | | 1789 | 1714 | 775.7 | 28.6 | 142.0 | νCO(R1) (69) + νCN(R1) (15) |
| 18 | 1658vs | 1650vs | 1733 | 1661 | 718.8 | 113.0 | 587.1 | νCO(R1) (75) |
| 19 | 1623vs | 1584s | 1634 | 1606 | 20.1 | 104.6 | 568.7 | νCC(R2) (64) + βCCH(R2) (21) |
| 20 | 1582s | | 1620 | 1592 | 288.9 | 71.8 | 395.3 | νCC(R1) (65) + νCN(R1) (18) |
| 21 | 1568s | | 1599 | 1571 | 2.7 | 4.6 | 25.5 | νCC(R2) (70) + βCCH(R2) (12) |
| 22 | 1519vs | | 1521 | 1495 | 26.2 | 2.4 | 14.6 | βCCH(R2) (58) + νCC(R2) (36) |
| 23 | | | 1509 | 1483 | 8.9 | 2.2 | 13.3 | $\delta_2CH_3$ (16C) (39) + $CH_{2rock}$ (13C) (23) + $\delta_1CH_3$ (16C) (13) |
| 24 | | | 1498 | 1473 | 3.6 | 10.8 | 66.0 | $\delta_1CH_3$ (16C) (76) + $\delta_2CH_3$ (16C) (11) |
| 25 | | | 1495 | 1469 | 40.6 | 13.2 | 80.9 | $\delta_2CH_3$ (30C) (37) + $CH_{2sciss}$ (13C) (14) + βCNH(R1) (11) |
| 26 | | 1463s | 1493 | 1468 | 144.8 | 25.6 | 157.3 | βCNH(R1) (34) + νCN(R1) (21) + $\delta_2CH_3$ (30C) (12) |
| 27 | | | 1492 | 1467 | 15.0 | 13.1 | 80.6 | $\delta_2CH_3$ (30C) (47) + $\delta_1CH_3$ (30C) (34) |
| 28 | | | 1488 | 1463 | 6.8 | 8.6 | 52.9 | $\delta_1CH_3$ (30C) (54) + $\delta_2CH_3$ (30C) (34) |
| 29 | 1431vs | | 1482 | 1456 | 23.2 | 24.3 | 151.2 | $CH_{2sciss}$ (10C) (72) |
| 30 | | | 1425 | 1401 | 5.3 | 1.2 | 7.5 | βCCH(R2) (44) + νCC(R2) (42) |
| 31 | 1397vs | | 1417 | 1393 | 223.4 | 2.2 | 14.2 | νCN(R1) (38) + βCCO(R1) (20) + νCC(R1) (12) + βCNH(R1) (10) |
| 32 | | 1408vs | 1416 | 1392 | 8.3 | 26.4 | 174.2 | $\delta CH_3$ (30C) (91) **Umbrella mode** |
| 33 | | | 1409 | 1385 | 1.5 | 0.2 | 1.0 | $\delta CH_3$ (16C) (91) **Umbrella mode** |
| 34 | | 1373 m | 1402 | 1378 | 2.9 | 11.5 | 76.7 | βCNH(R1) (71) + νCO(R1) (14) |
| 35 | 1351vs | 1349 m | 1385 | 1362 | 2.8 | 11.3 | 76.9 | $CH_{2wag}$(13C) (38) + $CH_{2wag}$ (10C) (36) + $\nu CC(CH_2)$ (18) |
| 36 | | 1309 m | 1341 | 1318 | 4.4 | 12.4 | 87.6 | $CH_{2twist}$ (10C) (41) + $CH_{2twist}$ (13C) (37) |
| 37 | 1311 m | | 1333 | 1310 | 2.0 | 2.5 | 17.8 | βCCH(R2) (69) + νCC(R2) (23) **Chubby Checker mode** |
| 38 | | | 1319 | 1296 | 0.1 | 1.3 | 9.5 | $CH_{2wag}$ (10 $CH_2$) (46) + $CH_{2wag}$ (13C) (29) |
| 39 | 1282vs | 1280vs | 1310 | 1288 | 0.7 | 0.9 | 6.62 | νCC(R2) (87) + βCCH(R2) (10) **Kekule mode** |
| 40 | | | 1295 | 1273 | 12.5 | 5.6 | 42.7 | $CH_{2twist}$ (13C) (25) + νCN(R1) (17) + $CH_{2twist}$ (10C) (17) |
| 41 | 1214vs | | 1239 | 1218 | 6.4 | 14.9 | 117.2 | νCN(R1) (23) + νCC(R1) (18) + $CH_{3rock2}$ (16C) (18) |
| 42 | | 1229vs | 1229 | 1208 | 8.2 | 22.1 | 175.3 | νCC(30C) (43) + νCC(R2) (24) + βCCH(R2) (16) + $\delta_{trig}$ (R2) (14) |
| 43 | 1196 m | | 1209 | 1188 | 60.2 | 3.8 | 30.3 | νCN(R1) (42) + $\nu CC(CH_2)$ (25) |
| 44 | 1185 m | 1180 m | 1207 | 1186 | 27.2 | 4.0 | 32.5 | βCCH(R2) (68) + νCC(R2) (18) |
| 45 | | | 1161 | 1141 | 23.7 | 7.1 | 60.7 | νCN(R1) (58) |
| 46 | 1117s | | 1136 | 1116 | 5.1 | 0.1 | 1.3 | βCCH(R2) (60) + νCC(R2) (33) |
| 47 | 1107w | 1095vs | 1109 | 1090 | 7.3 | 26.7 | 242.1 | $CH_{3rock1}$(16C) (31) + $\nu CC(CH_2)$ (20) |
| 48 | 1084s | 1089vs | 1105 | 1086 | 14.6 | 25.0 | 227.4 | νCC(R2) (30) + νCS (13) + $\nu CC(CH_2)$ (11)+ $CH_{3rock1}$ (16C) (10) **RBM (R2)** |
| 49 | | | 1093 | 1074 | 11.3 | 27.7 | 255.4 | νCC(R2) (20) + νCS (16) |
| 50 | 1030 m | | 1062 | 1044 | 7.8 | 0.1 | 1.3 | $CH_{2twist}$ (13C) (59) + γHCCC(R2) (12) |
| 51 | | 1028s | 1037 | 1020 | 0.7 | 5.0 | 49.6 | $\nu CC(CH_2)$ (94) |
| 52 | 1018 m | | 1033 | 1016 | 13.4 | 3.1 | 30.7 | $\delta_{trig}$ (R2) (65) + νCC(R2) (21) |
| 53 | | | 1017 | 999 | 25.6 | 10.4 | 105.4 | νCN(R1) (30) + $\delta_{trig}$ (R1) (28) + βCNH(R1) (10) |
| 54 | | | 1007 | 990 | 1.2 | 0.5 | 4.6 | $CH_{3rock1}$ (30C) (64)+ νCC(R2) (20) |
| 55 | 972w | | 993 | 976 | 0.1 | 0.1 | 0.4 | γHCCC(R2) (92) |
| 56 | 932 m | | 973 | 957 | 0.7 | 0.1 | 0.5 | γHCCC(R2) (81) + $\tau_{puck}$ (R1) (15) |
| 57 | | 913s | 908 | 893 | 22.4 | 10.3 | 120.1 | νCS(22) + νCN(R1) (13) + $\nu CC(CH_2)$ (11) |
| 58 | 885 m | 894w | 896 | 881 | 2.7 | 11.7 | 138.9 | νCC(R1) (22) + νCN(R1) (20) + νCC(10C−13C) (19) + $CH_{3rock1}$ (16C) (15) **RBM (R1)** |
| 59 | 842 m | 851w | 861 | 847 | 6.0 | 3.0 | 37.1 | $CH_{3rock2}$ (16C) (26) + $CH_{2rock}$ (10C) (12) + $CH_{2twist}$ (13C) (11) |
| 60 | 839 m | | 854 | 840 | 0.1 | 0.1 | 1.05 | γHCCC(R2) (100) |
| 61 | 817 m | | 831 | 816 | 34.7 | 0.3 | 3.7 | γHCCC(R2) (78) |
| 62 | | 794s | 812 | 798 | 1.2 | 29.0 | 389.3 | νCC(R2) (30) + νCC(30C) (23) + $\delta_2$(R2) (20) |
| 63 | 780s | | 799 | 786 | 5.9 | 0.9 | 11.9 | γNNCO(R1) (15) + νCC(9C−10C) (14) + νCC(R1) (12) |
| 64 | 760 m | 757 m | 760 | 747 | 5.5 | 1.1 | 15.5 | γNNCO (R1) (46) + $\tau_{puck}$ (R1) (16) |
| 65 | 735 m | | 750 | 737 | 40.8 | 0.0 | 0.2 | γNNCO(R1) (53) + $\tau_{puck}$ (R1) (27) + γCNCH(R1) (12) |
| 66 | | | 746 | 733 | 5.1 | 1.4 | 20.6 | τ(10C−13C) (21) + τ(13C−16C) (20) + $CH_{2rock}$ (13C) (18)+ $CH_{3rock2}$ (16C) (12) |
| 67 | 713 m | 703w | 724 | 712 | 2.3 | 0.2 | 2.5 | $\tau_{puck}$ (R2) (74) + γSCCC(R1) (10) |
| 68 | 647 m | | 667 | 656 | 75.3 | 1.0 | 18.0 | γCNCH(R1) (67) + γSCNC(R1) (10) |
| 69 | | | 652 | 641 | 8.6 | 1.1 | 19.0 | βCCO(R1) (50) |
| 70 | | 636w | 650 | 639 | 0.4 | 5.5 | 97.3 | $\delta_1$ (R2) (61) + $\delta_2$ (R2) (20) |
| 71 | 618 m | 627s | 629 | 618 | 0.7 | 3.5 | 65.4 | νCS(25) + βCCO(R1) (17) + νCC(30C) (12) + $\delta_2$ (R2) (11) |

**Table 7** (*continued*)

| S. No. | Experimental wavenumbers | | Calculated wavenumbers | | IR intensity | Raman Activity | Raman intensity | Assignment of dominant modes (PED below 10% not taken in to the consideration) |
|---|---|---|---|---|---|---|---|---|
| | FT-IR | Raman | Unscaled | Scaled | | | | |
| 72 | 580 m | 595s | 588 | 578 | 7.1 | 10.1 | 204.2 | νCN(R1) (18) + $\delta_2$ (R1) (16)+ γCCNS(R1) γSCNC(R1) (10) |
| 73 | | | 575 | 565 | 2.3 | 2.1 | 42.9 | γSCNC(R1) (33) + γCNCH(R1) (15) + $\tau_2$ (R1) (11) |
| 74 | 526 m | 528s | 548 | 538 | 22.3 | 2.7 | 59.1 | γCNCH(R1) (38) + $\delta_2$ (R1) (13) |
| 75 | | | 526 | 517 | 15.0 | 0.3 | 6.4 | $\tau_2$ (R2) (22) + γSCCC(R2) (17) + γCNCH(R1) (15) |
| 76 | 506w | | 515 | 506 | 24.5 | 2.1 | 50.2 | γCNCH(R1) (23) + γSCNC(R1) (15) + $\delta_1$ (R1) (11) |
| 77 | 436w | 443 m | 442 | 435 | 35.6 | 4.5 | 134.2 | $\delta_2$ (R1) (22) + νCS(18) + βCCO(R1) (17) |
| 78 | | 415 m | 420 | 412 | 0.2 | 0.1 | 2.57.6 | $\tau_2$ (R2) (62) + γHCCC(R2) (14) + $\tau_2$ (R2) (11) |
| 79 | 409w | | 414 | 407 | 1.7 | 0.8 | 25.3 | $\tau_2$ (R2) (17) + $\tau_1$ (R2) (13) + νCS(13) + $\delta_2$ (R2) (13) |
| 80 | | 385w | 381 | 375 | 5.9 | 2.2 | 82.0 | βCCO(R1) (39) + νCN(R1) (15) + νCS(14) |
| 81 | | | 375 | 368 | 3.6 | 0.9 | 35.2 | γCCCC(R1) (15) + γCNCH(R1) (13) + γCCNS(R1) (11) + $CCC_{sciss}$(10C) (10) |
| 82 | | | 371 | 365 | 0.4 | 0.3 | 11.8 | βCCC(R2) (50) + βCCH(R2) (18) |
| 83 | | | 330 | 325 | 1.7 | 1.8 | 81.8 | βC9CC(34) + τ(10C–13C) (12) |
| 84 | | 310 m | 300 | 295 | 0.3 | 3.9 | 205.0 | $CH_{2sciss}$ (13C) (27) + βCCO(R1) (10) + γSCCC(R1) (10) |
| 85 | | | 281 | 276 | 1.6 | 0.3 | 15.0 | $CH_{2sciss}$ (13C) (19) + τ(13C–16C) (15) + $\delta_1$ (R1) (10) |
| 86 | | | 242 | 238 | 0.4 | 0.1 | 7.9 | βCCH(R2) (64)+ βCCC(R2) (19) |
| 87 | | 239w | 237 | 233 | 0.1 | 0.5 | 34.5 | τ(13C–16C) (96) |
| 88 | | 194w | 189 | 186 | 0.1 | 5.1 | 555.3 | βCCO(R1) (28) + τ(13C–16C) (17) |
| 89 | | | 160 | 157 | 0.5 | 0.2 | 29.5 | $\delta_1$ (R2) (55) + γCNCH(R1) (29) |
| 90 | | | 151 | 148 | 0.8 | 0.5 | 72.2 | $\tau_2$ (R1) (32) + γCNCH(R1) (31) + $\tau_{puck}$ (R1) (26) |
| 91 | | | 139 | 137 | 1.1 | 0.4 | 68.7 | $\tau_{puck}$ (R1) (28) + γCNCH(R1) (21)+ $\delta_2$ (R2) (13) |
| 92 | | 110s | 121 | 119 | 1.6 | 0.2 | 48.0 | $\tau_{puck}$ (R1) (51) + γCNCH(R1) (25) + γCCCC(R1) (11) |
| 93 | | | 92 | 92 | 0.1 | 0.1 | 32.9 | τ(10C–13C) (58) + τ(9C–10C) (32) |
| 94 | | | 60 | 59 | 0.1 | 1.5 | 1275.1 | $\tau_1$ (R1) (27) + $\tau_2$ (R1) (26) + γCNCH(R1) (16) + $CCC_{sciss}$(10C) (10) |
| 95 | | | 51 | 50 | 0.3 | 2.9 | 3371.8 | τ(25C–30C) (48) + τ(9C–10C) (25) + τ(10C–13C) (12) |
| 96 | | | 43 | 42 | 0.2 | 0.6 | 1022.4 | τ(25C–30C) (98) |
| 97 | | | 37 | 37 | 0.4 | 4.0 | 8268.4 | τ(25C–30C) (80) |
| 98 | | | 35 | 35 | 0.2 | 5.6 | 12968.9 | τ(25C–30C) (69) + τ(1S–20C) (16) |
| 99 | | | 14 | 14 | 0.1 | 0.7 | 9005.8 | τ(4C–1S) (51) + τ(1S–20C) (16) + τ(25C–30C) (13) |

Abbreviations: R1-pyrimidine ring; R2-phenyl ring; ν-stretching, ss-symmetric, as-antisymmetric, as1 & as2-antisymmetric stretching; δ-deformation, δ1 & δ2-antisymmetric deformation; trig-trigonal; β-in plane bending; γ-out of plane bending; wag-wagging; rock-rocking; τ-torsion, τ1 & τ2-antisymmetric torsion; puck-puckering; sciss-scissoring; twist-twisting; RBM-ring breathing mode.

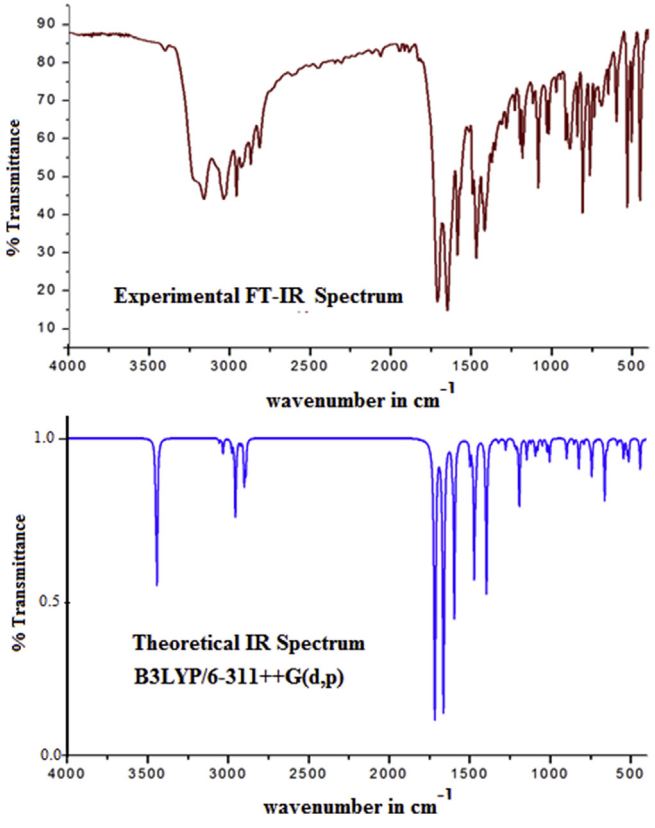


**Fig. 7.** The experimental FT-IR and theoretical IR spectra of $C_{14}H_{16}N_2O_2S$.

3222 $cm^{-1}$ in the FT-IR spectrum of the title compound is due to strong IR active N–H stretching mode, corresponding to the two N–H groups of the pyrimidine ring. The calculated scaled wavenumbers with strong IR intensity and 100% PED for the two N–H stretching modes are at 3452 and 3445 $cm^{-1}$. The red shift in the N–H stretching modes by 230 $cm^{-1}$ and 223 $cm^{-1}$ is due to the hydrogen bonding as predicted by the crystal structure [26]. The in plane/out of plane N–H bending modes have been assigned at wavenumbers 1468, 1378 $cm^{-1}$/656, 538 $cm^{-1}$, respectively.

### 4.7.2. C–S vibrations

Haress et al. [75] have reported, the bands at 676 $cm^{-1}$ in the IR spectrum, 663, 640 $cm^{-1}$ in the Raman spectrum and at 674, 665, 643, 614 $cm^{-1}$ in theoretical spectrum as the C–S stretching modes. Kaur et al. [76] reported the C–S stretching modes at 672 $cm^{-1}$ in the IR spectrum, 674 $cm^{-1}$ in the Raman spectrum and the theoretically calculated values at 696 and 671 $cm^{-1}$. The C–S stretching mode is reported at about 641 $cm^{-1}$ (IR), 645 (Raman) and 704, 640 (DFT) by Mary et al. [77]. Similar mode has been observed at about 640 $cm^{-1}$ by Cravino et al. [78]. In the present study, as the sulfur atom is bridged between the phenyl and pyrimidine ring, the C–S stretching vibration is observed at a slightly higher value at 913 $cm^{-1}$ in addition to the peak at 627 $cm^{-1}$ in the FT-Raman spectrum while the theoretically calculated values are assigned at wavenumbers 893 and 618 $cm^{-1}$ for C–S stretching vibration. The out of plane bending vibrations are observed at 565 and 517 $cm^{-1}$ theoretically.

### 4.7.3. C=O vibrations

The appearance of strong bands around 1800–1650 $cm^{-1}$ in the FT-IR spectrum mark the presence of carbonyl group and attributable to the C=O stretching motion [79]. The position of this band

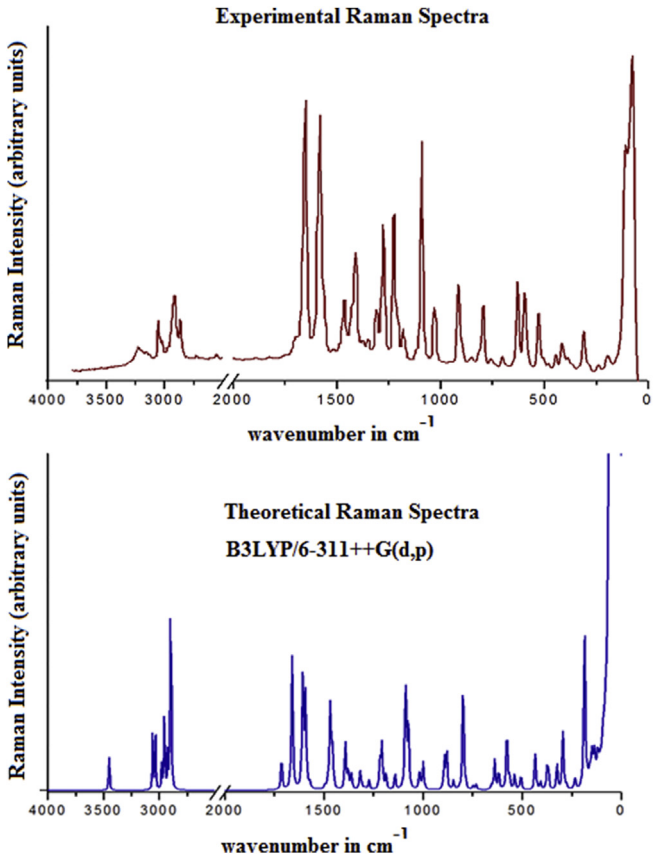


**Fig. 8.** The experimental FT-Raman and theoretical Raman spectra of $C_{14}H_{16}N_2O_2S$.

within this wavenumber range depends on the molecular environment of the C═O group. The two C═O groups of the title compound give rise to two strong bands at 1709 and 1658 $cm^{-1}$ in the FT-IR spectrum with DFT calculated value at 1714 and 1661 $cm^{-1}$. The studies of Pavel et al. [80] and Palafox et al. [81] on uracil derivatives, support our assignment. Not only the C═O stretching, in-plane and out of plane bending of carbonyl group is also observed to be sensitive to its proximity with other groups. Prasad et al. [82] have reported the C═O in-plane and out-of-plane bending at 615 and 595 $cm^{-1}$ respectively, for 1H-indene-1,3(2H)-dione. The in-plane and out-of-plane C═O bending modes for 2-methylacetoacetanilide at B3LYP/6−311++G(d,p) have been reported at 845 and 693 $cm^{-1}$ by Arjunan et al. [83]. The in-plane in-phase C═O vibration of the two C═O groups is computed at 641 and in-plane out-of-phase C═O vibration at 375 $cm^{-1}$ well matched at 385 $cm^{-1}$ in the FT-Raman spectrum. The C═O out-of-plane bending modes were calculated at 747 and 737 $cm^{-1}$ and assigned with the medium band at 757 $cm^{-1}$ in the FT-Raman and 760 and 735 $cm^{-1}$ in the FT-IR spectrum.

*4.7.4. Phenyl ring vibrations*

The phenyl ring spectral region chiefly comprises of C–H, C–C and C═C stretching, and the C–C–C as well as H–C–C-bending vibrations. The bands due to the ring C–H-stretching vibrations were observed as a group of partially overlapping absorptions in the region 3100–3000 $cm^{-1}$. The calculated wavenumbers in the region 3059–3033 $cm^{-1}$ are identified as the C–H stretching modes and have been assigned at 3061, 3035, 3033 $cm^{-1}$/3058, 3054 $cm^{-1}$ in the experimental FT-IR/FT-Raman spectrum, respectively. The vibrations involving the C–H in-plane bending were found within the region 1606–1116 $cm^{-1}$. The ring C–C stretching vibrations usually occur in the region 1625–1430 $cm^{-1}$ [84]. For the title compound, calculated bands at 1606, 1571 1495 and 1310 $cm^{-1}$ are due to C–C stretching of ring. The interesting Chubby Checker mode of the ring calculated at 1310 $cm^{-1}$ was experimentally well matched with the medium intensity band in FT-IR spectrum at 1311 $cm^{-1}$. The Kekule and the ring breathing modes were observed at 1282/1280 and 1084/1089 $cm^{-1}$ in FT-IR/FT-Raman spectra, respectively. The trigonal ring deformation is calculated wavenumber at 1016 $cm^{-1}$. The dominant C–H out-of-plane bending modes at 976 and 840 $cm^{-1}$ are found to have contributions more than 90% to the total PED and are assigned well at 972 and 839 $cm^{-1}$ peaks in the experimental FT-IR spectrum. The torsional modes generally appear in the low wavenumber regions. In the present case, the calculated normal modes below 565 $cm^{-1}$ wavenumbers are mainly the torsional modes. The phenyl ring torsional modes are calculated at 517, 412 and 407 $cm^{-1}$ and the corresponding peak has been observed experimentally at 415 $cm^{-1}$ in the FT-Raman and 409 $cm^{-1}$ in FT-IR spectra.

*4.7.5. $CH_2$ vibrations*

The title compound has two methylene groups ($C10H_2$ and $C13H_2$), attached between the pyrimidine ring and terminal methyl group (Fig. 1). The $CH_2$ group vibrations show anti-symmetric and symmetric stretching, scissoring, rocking, wagging and twisting vibrational motions. The anti-symmetric $CH_2$ stretching vibrations are generally observed in the region 3100–3000 $cm^{-1}$, while the symmetric stretch appears between 3000 and 2900 $cm^{-1}$. The calculated $CH_2$ anti-symmetric stretching vibrations were identified at 2943, 2926 $cm^{-1}$ and symmetric vibrations are found at 2902 and 2894 $cm^{-1}$ (observed at 2925 $cm^{-1}$ in FT-IR). The $CH_2$ scissoring vibrations appear normally in the region 1490–1435 $cm^{-1}$ as medium intense bands [85]. In the title compound, the dominant $CH_2$ scissoring mode is calculated at 1456 $cm^{-1}$ with 72% to total PED contribution which corresponds to a very strong peak at 1431 $cm^{-1}$ in FT-IR spectrum. The wavenumbers calculated at 1362 and 1296 $cm^{-1}$ are assigned to the methylene wagging modes, well matched with experimental FT-IR band at 1351 $cm^{-1}$ and FT-Raman at 1349 $cm^{-1}$. In the present assignments, the general trend for the wavenumber of $CH_2$ bending modes is observed i.e. wavenumbers increase as we go from rocking→ twisting→ wagging→ scissoring of the methylene group. The twisting modes are predicted at 1318, 1273 and 1044 $cm^{-1}$, while the rocking modes of the methylene group are mixed modes and have been calculated at 847 and 733 $cm^{-1}$.

*4.7.6. Methyl group vibrations*

The title compound possesses two $CH_3$ groups ($C30H_3$ and $C16H_3$). Nine fundamentals can be associated to each C–$CH_3$ group [86]. The C–H stretching of the methyl group occurs at lower frequencies than those of aromatic ring. Moreover, the antisymmetric stretch is usually at higher wavenumber than the symmetric stretch. For compounds containing $CH_3$ group, the symmetric C–H stretching mode appears in the range 2935–2860 $cm^{-1}$, whereas the anti-symmetric stretching modes appear in the region 2985–2925 $cm^{-1}$ [87]. In this present study, the symmetric stretching vibrations for the two methyl groups are calculated at 2901 and 2891 $cm^{-1}$, whereas the $CH_3$ anti-symmetric modes are assigned in the range 2980–2953 $cm^{-1}$. The experimental peak for the anti-symmetric $CH_3$ stretch is at 2957 and 2953 $cm^{-1}$ (FT-IR) and for symmetric stretch are at 2919, 2866 (Raman) and 2852 $cm^{-1}$ (FT-IR). The anti-symmetric and symmetric deformation vibrations of the methyl group usually appear within the region 1465–1440 $cm^{-1}$ and 1390–1370 $cm^{-1}$ [88]. In the present investigation, the wavenumbers corresponding to the two asymmetric deformations are assigned at 1483, 1473 for $C16H_3$ and 1467,

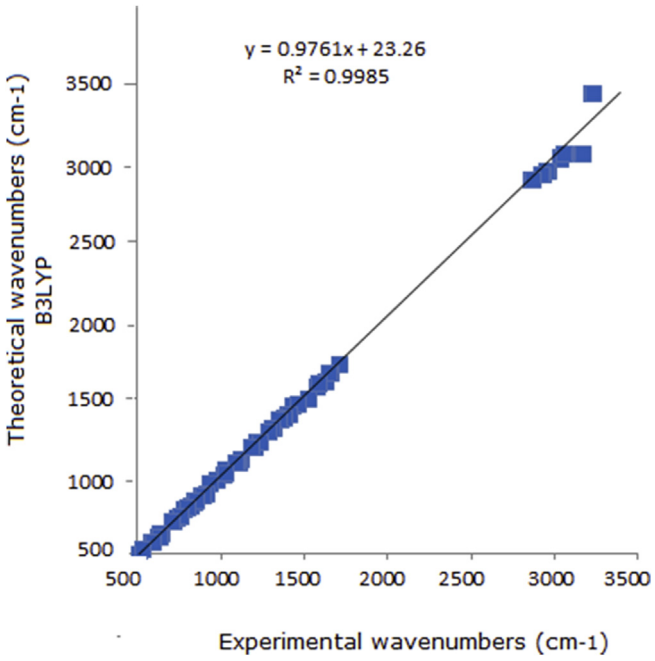


**Fig. 9.** Correlation graphics of experimental and theoretical (scaled) wavenumbers of the title compound.

1463 $cm^{-1}$ for C30$H_3$. The band around 1390 $cm^{-1}$ in FT-Raman is usually characteristic for the umbrella mode of the methyl group [89]. Meanwhile, the calculated wavenumbers at 1392 and 1385 $cm^{-1}$ have been assigned as the symmetric deformation (umbrella mode) with >90% contribution to PED. The methyl rocking mode usually appears within the region 1070–1010 $cm^{-1}$ [90,91]. The strong band at 1095 $cm^{-1}$ in Raman spectrum is due to the C16$H_3$ rocking vibrational motion with theoretical peak at 1090 and the peak for C30H3 rocking is at 990 $cm^{-1}$. As the wavenumber for the A-$CH_3$ rocking vibration depends on the electronegativity of 'A' atom, and increases with increasing electronegativity, these modes are in line with charges of the C13 and C25 attached to the two methyl groups as given in Table S1.

All the calculated vibrational wavenumbers are in fair agreement with the experimental wavenumbers. The correlation graphic which shows accord between the calculated and experimental wavenumbers is shown in Fig. 9. As seen from the figure, the experimental fundamentals have a good correlation at B3LYP level.

## 5. Conclusions

In the present communication, we have presented the calculation of molecular properties and vibrational analysis of the title compound, at the DFT level of theory using FT-IR and FT-Raman spectroscopic information. The present study emphasizes the effectiveness of B3LYP method when used with proper basis set to accurately replicate the band positions and relative intensities of the vibrational bands even for large molecules. The red shift in the N–H stretching modes is due to the N–H···O=C hydrogen bonding. The pyrimidine ring breathing is highly sensitive to the environment, interaction and substitution and is calculated at 881 $cm^{-1}$ in good coherence with experimental peak at 885 (FT-IR)/894 (FT-Raman) $cm^{-1}$. The hyperpolarizabilty of the title compound is calculated to be 3.3775 $\times$ $10^{-30}$ e.s.u. The dipole moment (6.626 Debye) as well as polarizabilty (31.9091 $\times$ $10^{-24}$ e.s.u.) is found to be quite high. The strong hydrogen bonding present in the crystal structure is manifested by the strength of the hydrogen bond (5.05596 kcal/mol) calculated using counterpoise correction method.

## Acknowledgments

The authors would like to extend their sincere appreciation to the Deanship of Scientific Research at King Saud University for funding this work through the Research Group Project No. PRG-1436-23.

## Appendix A. Supplementary data

Supplementary data related to this article can be found at http://dx.doi.org/10.1016/j.molstruc.2015.07.042.

## References

[1] K. Ghoshal, S.T. Jacob, Biochem. Pharmacol. 53 (1997) 1569–1575.
[2] R.S. Klein, M. Lenzi, T.H. Lim, K.A. Hotchkiss, P. Wilson, E.L. Schwartz, Biochem. Pharmacol. 62 (2001) 1257–1263.
[3] O.N. Al-Safarjalani, X. Zhou, R.H. Rais, J. Shi, R.F. Schinazi, F.N.M. Naguib, M.H. El Kouni, Cancer Chemother. Pharmacol. 55 (2005) 541–551.
[4] N. Sirisoma, S. Kasibhatla, B. Nguyen, A. Pervin, Y. Wang, G. Claassen, B. Tseng, J. Drewe, S.X. Cai, Bioorg. Med. Chem. 14 (2006) 7761–7773.
[5] M. Artico, S. Massa, A. Mai, M.E. Marongiu, G. Piras, E. Tramontino, P. La Colla, Antivir. Chem. Chemother. 4 (1993) 361–368.
[6] R. Ragno, A. Mai, S. Sbardella, M. Artico, S. Massa, C. Musiu, M. Mura, T. Marceddu, A. Cadeddu, P. La Colla, J. Med. Chem. 47 (2004) 928–934.
[7] X. Lu, Y. Chen, Y. Guo, Z. Liu, Y. Shi, Y. Xu, X. Wang, Z. Zhang, J. Liu, Bioorg. Med. Chem. 15 (2007) 7399–7407.
[8] A.A. El-Emam, M.A. Massoud, E.R. El-Bendary, M.A. El-Sayed, Bull. Kor. Chem. Soc. 25 (2004) 991–996.
[9] N.R. El-Brollosy, O.A. Al-Deeb, A.A. El-Emam, E.B. Pedersen, P. La Colla, G. Collu, G. Sanna, L. Roberta, Arch. Pharm. 342 (2009) 663–670.
[10] M.N. Brunelle, J. Lucifora, J. Neyts, S. Villet, A. Holy, C. Trepo, F. Zoulim, Antimicrob. Agents Chemother. 51 (2007) 2240–2243.
[11] R. Kumar, W. Semaine, M. Johar, D.L.J. Tyrrell, B. Agrawal, J. Med. Chem. 49 (2006) 3693–3700.
[12] Y. Ding, J.L. Girardet, K.L. Smith, G. Larson, B. Prigaro, J.Z. Wu, N. Yao, Bioorg. Chem. 34 (2006) 26–38.
[13] K.K. Gauni, H. Kohlhage, Chemotherapy 14 (1969) 158–169.
[14] P. Russ, P. Schelling, L. Scapozza, G. Folkers, E. De Clercq, V.E. Marquez, J. Med. Chem. 46 (2003) 5045–5054.
[15] W. Brumfitt, J.M. Hamilton-Miller, J. Chemother. 5 (1993) 465–469.
[16] H.H. Locher, H. Schlunegger, P.G. Hartman, P. Anghern, R.L. Then, Antimicrob. Agents Chemother. 40 (1996) 1376–1381.
[17] C.A. Sincak, Ann. Pharmacother. 43 (2009) 1107–1114.
[18] E.S. Al-Abdullah, A.R. Al-Obaid, O.A. Al-Deeb, E.E. Habib, A.A. El-Emam, Eur. J. Med. Chem. 46 (2011) 4642–4647.
[19] E.S. Al-Abdullah, A.A. Al-Turkistani, O.A. Al-Deeb, N.R. El-Brollosy, E.E. Habib, A.A. El-Emam, Drug Res. 64 (2014) 31–39.
[20] D. Tassel, M.A. Madoff, J. Am. Med. Assoc. 206 (1968) 830–832.
[21] A. Mai, D. Rotili, S. Massa, G. Brosch, G. Simonetti, C. Passariello, A. Palamara, Bioorg. Med. Chem. Lett. 17 (2007) 1221–1225.
[22] A.F. Cowman, M.J. Morry, B.A. Biggs, G.A. Cross, S.J. Foote, Proc. Natl. Acad. Sci. U. S. A. 85 (1988) 9109–9113.
[23] A. Sardarian, K.T. Douglas, M. Read, P.F.G. Sims, J.E. Hyde, P. Chitnumsub, R. Sirawaraporn, W. Sirawaraporn, Org. Biomol. Chem. 1 (2003) 960–964.
[24] C. Sirichaiwat, C. Intaraudom, S. Kamchonwongpaisan, J. Vanichtanankul, Y. Thebtaranonth, Y. Yuthavong, J. Med. Chem. 47 (2004) 345–354.
[25] B.K. Singh, M. Mishra, N. Saxena, G.P. Yadav, P.R. Maulik, M.K. Sahoo, R.L. Gaur, P.K. Murthy, R.P. Tripathi, Eur. J. Med. Chem. 43 (2008) 2717–2723.
[26] T. Miyasaka, H. Tanaka, M. Baba, H. Hayakawa, R.T. Walker, J. Balzarini, E. De Clercq, J. Med. Chem. 32 (1989) 2507–2509.
[27] H. Tanaka, H. Takashima, M. Ubasawa, K. Sekiya, I. Nitta, M. Baba, S. Shigeta, R.T. Walker, E. De Clercq, T. Miyasaka, J. Med. Chem. 35 (1992) 337–345.
[28] H. Tanaka, H. Takashima, M. Ubasawa, K. Sekiya, I. Nitta, M. Baba, S. Shigeta, R.T. Walker, E. De Clercq, T. Miyasaka, J. Med. Chem. 35 (1992) 4713–4719.
[29] R. Pontikis, R. Benhida, A.H. Aubertin, D.S. Grieson, C. Monneret, J. Med. Chem. 40 (1997) 1845–1854.
[30] A.L. Hopkins, J. Ren, R.M. Esnouf, B.E. Willcox, E.Y. Jones, C. Ross, T. Miyasaka, R.T. Walker, H. Tanaka, D.K. Stammers, D.I. Stuart, J. Med. Chem. 39 (1996) 1589–1600.
[31] M.I. Attia, A.A. El-Emam, A.A. Al-Turkistani, A.L. Kansoh, N.R. El-Brollosy, Molecules 19 (2014) 279–290.
[32] N.Z. Alzoman, Y.S. Mary, C.Y. Panicker, I.A. Al-Swaidan, A.A. El-Emam, O.A. Al-Deeb, A.A. Al-Saadi, C. Van Alsenoy, J.A. War, Spectrochim. Acta A 139 (2015) 413–424.
[33] N.G. Haress, A.A. El-Emam, O.A. Al-Deeb, C.Y. Panicker, A.A. Al-Saadi, C. Van Alsenoy, J.A. War, S.K. Srivastava, Spectrochim. Acta A 137 (2015) 569–580.

[34] E.S. Al-Abdullah, Y.S. Mary, C.Y. Panicker, N.R. El-Brollosy, A.A. El-Emam, C. Van Alsenoy, A.A. Al-Saadi, Spectrochim. Acta A 133 (2014) 639–650.
[35] Y. Sert, A.A. El-Emam, O.A. Al-Deeb, A.A. Al-Turkistani, Ç. Çirak, F. Ucun, Spectrochim. Acta A 126 (2014) 86–97.
[36] F.A.M. Al-Omary, H.A. Ghabbour, A.A. El-Emam, C.S. Chidan Kumar, H.-K. Fun, Acta Cryst. E70 (2014) o179–o180.
[37] A.D. Becke, J. Chem. Phys. 98 (1993) 5648–5652.
[38] C. Lee, W. Yang, R.G. Parr, Phys. Rev. B 37 (1998) 785–789.
[39] S.F. Boys, F. Bernardi, Mol. Phys. 19 (1970) 553–566.
[40] A.D. Buckingham, Adv. Chem. Phys. 12 (1967) 107–142.
[41] D.R. Kanis, M.A. Ratner, T.J. Marks, Chem. Rev. 94 (1994) 195–242.
[42] R. Ditchfield, J. Chem. Phys. 56 (1972) 5688–5691.
[43] K. Wolinski, J.F. Hinton, P. Pulay, J. Am. Chem. Soc. 112 (1990) 8251–8260.
[44] E.D. Glendening, C.R. Landis, F. Weinhold, Comput. Mol. Sci. 2 (2012) 1–42.
[45] M.J. Frisch, G.W. Trucks, H.B. Schlegel, G.E. Scuseria, M.A. Robb, J.R. Cheeseman, G. Scalmani, V. Barone, B. Mennucci, G.A. Petersson, H. Nakatsuji, M. Caricato, X. Li, H.P. Hratchian, A.F. Izmaylov, J. Bloino, G. Zheng, J.L. Sonneberg, M. Hada, M. Ehara, K. Toyota, R. Fukuda, J. Hasegawa, M. Ishida, T. Nakajima, Y. Honda, O. Kitao, H. Nakai, T. Vreven, J.A. Montgomery, J.E. Peralta, F. Ogliaro, M. Bearpark, J.J. Heyd, E. Brothers, K.N. Kudin, V.N. Staroverov, T. Keith, R. Kobayashi, J. Normand, K. Raghavachari, A. Rendell, J.C. Knox, J.B. Cross, V. Bakken, C. Adamo, J. Jaramillo, R. Gomperts, R.E. Stratmann, O. Yazyev, A.J. Austin, R. Cammi, C. Pomelli, J.W. Ochterski, R.L. Martin, K. Morokuma, V.G. Zakrzewski, G.A. Voth, P. Salvador, J.J. Dannenberg, S. Dapprich, A.D. Daniels, O. Farkas, J.B. Foresman, J.V. Ortiz, J. Cioslowski, D.J. Fox, Gaussian 09, Revision A.1, Gaussian, Inc, Wallingford CT, 2009.
[46] G. Socrates, Infrared and Raman Characteristic Frequencies, third ed., John Wiley & Sons Ltd., Chichester, 2001.
[47] P. Pulay, G. Fogarasi, G. Pongor, J.E. Boggs, A. Vargha, J. Am. Chem. Soc. 105 (1983) 7037–7047.
[48] E. Frisch, H.P. Hratchian, R.D. Dennington II, T.A. Keith, John Millam, B. Nielsen, A.J. Holder, J. Hiscocks, GaussView Version 5.0.8, Gaussian, Inc., 2009.
[49] T. Sundius, J. Mol. Spectrosc. 82 (1980) 138–151.
[50] T. Sundius, J. Mol. Struct. 218 (1990) 321–336.
[51] T. Sundius, Vib. Spectrosc. 29 (2002) 89–95.
[52] M. Karabacak, M. Kurt, M. Cinar, A. Coruh, Mol. Phys. 107 (2009) 253–264.
[53] N. Sundaraganesan, S. Ilakiamani, H. Saleem, P.M. Wojciechowski, D. Michalska, Spectrochim. Acta A 61 (2005) 2995–3001.
[54] J.B. Foresman, A. Frisch, Exploring Chemistry with Electronic Structure Methods, second ed., Gaussian Inc., Pittsburgh, PA, 1996.
[55] G. Keresztury, S. Holly, J. Varga, G. Besenyei, A.Y. Wang, J.R. Durig, Spectrochim. Acta A 49 (1993) 2007–2017.
[56] G. Keresztury, Raman spectroscopy: theory, in: J.M. Chalmers, P.R. Griffith (Eds.), Handbook of Vibrational Spectroscopy vol. 1, John Wiley & Sons, New York, 2002, pp. 71–87.
[57] I. Fleming, Frontier Orbitals and Organic Chemical Reactions, John Wiley & Sons, New York, 1976.
[58] J.S. Murray, K. Sen, Molecular Electrostatic Potentials, Concepts and Applications, Elsevier, Amsterdam, 1996.
[59] I. Alkorta, J.J. Perez, Int. J. Quant. Chem. 57 (1996) 123–135.
[60] E. Scrocco, J. Tomasi, in: P. Lowdin (Ed.), Advances in Quantum Chemistry, Academic Press, New York, 1978.
[61] F.J. Luque, M. Orozco, P.K. Bhadane, S.R. Gadre, J. Phys. Chem. 97 (1993) 9380–9384.
[62] J. Sponer, P. Hobza, Int. J. Quant. Chem. 57 (1996) 959–970.
[63] S.R. Gadre, I.H. Shrivastava, J. Chem. Phys. 94 (1991) 4384–4390.
[64] N.M. O'Boyle, A.L. tenderholt, K.M. langer, J. Comput. Chem. 29 (2008) 839–845.
[65] M. Szafran, A. Komasa, E.B. Adamska, J. Mol. Struct. Theochem. 827 (2007) 101–107.
[66] T. Schlick (Ed.), Molecular Modeling and Simulation: an Interdisciplinary Guide, second ed. vol. 21, Springer, New York, 2010.
[67] V.P. Gupta, Archna Sharma, Ajit Virdi, Vishnuji Ram, Spectrochim. Acta A 64 (2006) 57–67.
[68] Y. Sert, M. Mahendra, K. Chandra, K.B. Shivashankar, H. Puttaraju, Ç. Doğan, F. Çırak, Ucun, Spectrochim. Acta A 128 (2014) 109–118.
[69] A.J. Barnes, M.A. Stuckey, L. Le Gall, Spectrochim. Acta A 40 (1984) 419–431.
[70] R.A. Yadav, P.N.S. Yadav, J.S. Yadav, Spectrochim. Acta A 44 (1988) 1201–1206.
[71] C. Bayrak, J. Biol. Chem. 41 (2013) 133–141.
[72] D.K. Singh, S. Mishra, A.K. Ojha, S.K. Srivastava, S. Schlucker, B.P. Asthana, J. Popp, R.K. Singh, J. Raman, Spectrosc. 42 (2011) 667–675.
[73] G. Gunasekaran, E. Sailatha, Indian J. Pure Appl. Phys. 47 (2009) 259–264.
[74] J.S. Singh, Pramana-J. Phys. 70 (2008) 479–486.
[75] N.G. Haress, A.A. El-Emam, O.A. Al-Deeb, C.Y. Panicker, A.A. Al-Saadi, C. Van Alsenoy, J.A. War, S.K. Srivastava, Spectrochim. Acta A 137 (2015) 569–580.
[76] M. Kaur, Y.S. Mary, C.Y. Panicker, H.T. Varghese, H.S. Yathirajan, K. Byrappa, C. Van Alsenoy, Spectrochim. Acta A 120 (2014) 445–455.
[77] Y.S. Mary, K. Raju, I. Yildiz, O. Temiz-Arpaci, H.I.S. Nogueira, C.M. Granadeiro, C. Van Alsenoy, Spectrochim. Acta A 96 (2012) 617–625.
[78] A. Cravino, H. Neugebauer, S. Luzzati, M. Catellani, N.S. Sariciftci, J. Phys. Chem. 105 B (2001) 46–52.
[79] M. Karabacak, L. Sinha, O. Prasad, Z. Cinar, M. Cinar, Spectrochim. Acta A 93 (2012) 33–46.
[80] I. Pavel, S. Cota, S. Cinta-Pinzaru, W. Kiefer, J. Phys. Chem. A 109 (2005) 9945–9952.
[81] M.A. Palafox, G. Tardajos, A. Guerrero-Martínez, J.K. Vats, H. Joe, V.K. Rastogi, Spectrochim. Acta A 75 (2010) 1261–1269.
[82] O. Prasad, L. Sinha, N. Misra, V. Narayan, N. Kumar, J. Pathak, J. Mol. Struct. Theochem. 940 (2010) 82–86.
[83] V. Arjunan, M. Kalaivani, S. Senthilkumari, S. Mohan, Spectrochim. Acta A 115 (2013) 154–174.
[84] M. Karabacak, E. Yilan, Spectrochim. Acta A 87 (2012) 273–285.
[85] L.J. Bellamy, The Infrared Spectra of Complex Molecules, second ed., Chapman and Hall, London, 1980.
[86] P.S. Kalsi, Spectroscopy of Organic Compounds, Wiley Eastern Limited, New Delhi, 1993.
[87] N. Sundaraganesan, C. Meganathan, H. Saleem, B. Dominic Joshua, Spectrochim. Acta A 68 (2007) 619–625.
[88] J. Mohan, Organic Spectroscopy – Principles Applications, Narosa Publishing House, New Delhi, 2001.
[89] A.-M.S. Al-Tamimi, A.A. El-Emam, O.A. Al-Deeb, O. Prasad, S.K. Pathak, R. Srivastava, L. Sinha, Spectrochim. Acta A 124 (2014) 108–123.
[90] A. Altun, K. Golcuk, M. Kumru, J. Mol. Struct. Theochem. 637 (2003) 155–169.
[91] H. Endredi, F. Billes, G. Keresztury, J. Mol. Struct. Theochem. 677 (2004) 211–225.